Rapid Communications

Simulation of live-cell imaging system reveals hidden uncertainties in cooperative binding measurements

Masaki Watabe,[1,*] Satya N. V. Arjunan,[1,2] Wei Xiang Chew,[1,3] Kazunari Kaizu,[1] and Koichi Takahashi[1,4,5,†]

[1]*Laboratory for Biologically Inspired Computing, RIKEN Center for Biosystems Dynamics Research, Suita, Osaka 565-0874, Japan*

[2]*Lowy Cancer Research Centre, The University of New South Wales, Sydney, Australia*

[3]*Physics Department, Faculty of Science, University of Malaya, Kuala Lumpur 50603, Malaysia*

[4]*Institute for Advanced Biosciences, Keio University, Fujisawa, Kanagawa 252-8520, Japan*

[5]*Department of Biosciences and Informatics, Keio University, Yokohama, Kanagawa 223-8522, Japan*

(Received 4 October 2018; published 3 July 2019)

We propose a computational method to quantitatively evaluate the systematic uncertainties that arise from undetectable sources in biological measurements using live-cell imaging techniques. We then demonstrate this method in measuring the biological cooperativity of molecular binding networks, in particular, ligand molecules binding to cell-surface receptor proteins. Our results show how the nonstatistical uncertainties lead to invalid identifications of the measured cooperativity. Through this computational scheme, the biological interpretation can be more objectively evaluated and understood under a specific experimental configuration of interest.

DOI: 10.1103/PhysRevE.100.010402

Introduction. Recent progress in robotic and automated techniques for sampling and analyzing complex biological data can reduce statistical uncertainties, increasing precision in measuring biological and physical properties in living cells [1–4]. However, despite advances in computational techniques, the measurement process has resisted the quantitative evaluation of systematic uncertainties that arise from inaccuracies in experimental data acquisition and analysis [5,6]. An absence and ignorance of the evaluation of such systematic uncertainties often lead to excessive interpretations of the measured properties.

A key challenge to evaluating the systematic uncertainties is finding a meaningful and nonintuitive variance. There exist a large number of systematic sources in the measurement processes, but no well-defined procedure to evaluate systematic variance. Although experienced experimental biophysicists are able to anticipate some systematic sources (e.g., the faulty calibration of measurement equipment) and ensure that most systematic uncertainties are much less than the required precision, other sources cannot even be detected by empirical approaches. The systematic variance that arises from undetectable sources in the measurement process can cause erroneous identification and interpretation of measured properties [5–8]. For example, structural uncertainties that arise from various model assumptions in biological network topologies cannot be directly extracted from experimental data, introducing errors into analysis and potentially giving rise to misleading conclusions [9,10]. Thus, the measurement processes require a nonexperimental evaluation method that allows biophysicists to objectively interpret the measured outputs and draw proper conclusions.

To better understand the origin of these hidden uncertainties, we consider a process of data-driven (or inductive) modeling in bioimaging. For the sake of simplicity, we assume modeling the steady state behavior of a specific type of protein (e.g., cell-membrane receptors) in a living cell of interest. In this modeling, we also assume that a fluorescence microscopy system measures the concentrations of the proteins tagged with fluorescent emitters (e.g., green fluorescence proteins) within the focal plane of the optics onto a digital camera placed at the conjugated focal plane. Technical details of extracting the protein concentrations from microscopy images are also omitted in this simplification.

Here, as an example, we evaluate the systematic uncertainties associated with a specific parameter (e.g., image acquisition periods) in the simplified measurement process. We first consider that the measured concentration of the observed proteins is a function of time at the ith image frame $C(t_i)$. For m cell samples, the experimenters ensure the stability of the concentration changes in an image acquisition period T. The observed rate in the protein concentrations converges near 0 as $t_i \to T$,

$$\frac{\Delta C_i}{\Delta t_i} \to 0 \pm \sigma_{C'}, \tag{1}$$

where $\Delta C_i = C(t_i) - C(t_{i-1})$ and $\Delta t_i = t_i - t_{i-1}$ are the concentration and time difference at the ith image frame, respectively. $\sigma_{C'}$ represents the statistical deviations in the observed rates. An "apparent" steady state of the protein concentrations is then computed by the time-average integration $\overline{C} \pm \sigma_{\overline{C}}$.

In the data-driven approach, the measured protein concentrations are typically fitted to the network model constructed under the data interpretation that the measured concentrations

*masaki@riken.jp
†ktakahashi@riken.jp

fully converge to equilibrium within the acquisition period. The rate of concentration changes in the observed proteins interacting with N variables can be theoretically modeled in the form of an ordinary differential equation. In equilibrium modeling, the rate fully converges to 0 as $t \to \infty$,

$$\frac{dR(t)}{dt} = f(R(t), \mathbf{x}(t), t; \theta) \to 0, \tag{2}$$

where $R(t)$ is the observed protein concentration as a function of time and model parameters θ (e.g., dissociation constants), $\mathbf{x}(t) = [x_1(t), \ldots, x_N(t)]$, and $x_i(t)$ is the value of the ith variable at t and θ. In the equilibrium modeling, the rate of changes in the ith variable over time also fully converges to 0 as $t \to \infty$, $dx_i(t)/dt = f_i(R(t), \mathbf{x}(t), t; \theta) \to 0$. The full-equilibrium concentration in the observed proteins is then computed by the time-average integration $\widetilde{R}(\theta) = \lim_{\tau\to\infty} \frac{1}{\tau} \int_0^\tau R(t;\theta)dt$. Fitting procedures (e.g., maximum-likelihood method) directly compare the measured concentration ($\overline{C}$) to the theoretical full-equilibrium concentration [$\widetilde{R}(\theta)$] binned into each histogram. The best-fit model parameters ($\overline{\theta}$) are those which minimize the discrepancies defined in an optimization function $\mathcal{M}(\widetilde{R}(\theta), \overline{C}, \sigma_{\overline{C}})$. Confidence levels and correlations are also estimated in each fitting parameter.

Although the experimenters ensure the stability of the measured protein concentration changes in time and show the goodness of fit to the equilibrium model, actual biological cells generally operate out of equilibrium. In Eq. (1), the apparent state stability can be not only interpreted as the complete convergence of the protein responses to full equilibrium but also the incomplete convergence if the responses are so slow that the protein concentration remains nonequilibrium during the acquisition period. To split these double data interpretations, the experimenters, however, must contend with the experimental configuration and the state-transition speed in the observed proteins. The data interpretation that gives rise to the complete convergence requires not only maximizing event samples in a shorter image acquisition period but also fastens the observed rates of converging to the full equilibrium. The configuration to reduce statistical uncertainties constrains the limitation and sensitivity in measuring the state-transition time. Because of these tradeoffs, it is unclear when or whether the measured protein concentration actually converges to the full equilibrium within the acquisition period T.

To see the effects of the double data interpretations in the apparent steady states, we consider a Taylor expansion of Eq. (2) at the model-true equilibrium concentration $\overline{R} = \widetilde{R}(\overline{\theta})$,

$$f(R(t;\overline{\theta})) \approx [R(t;\overline{\theta}) - \overline{R}] \frac{\partial f}{\partial R}\bigg|_{R(t;\overline{\theta})=\overline{R}} + \cdots, \tag{3}$$

where the zeroth-order term vanishes at the model-true equilibrium $f(\overline{R}) = 0$. At $t = T$, we evaluate the systematic variance that arises from the following model assumptions. If full equilibrium is proper as a model assumption, then $f(R(T;\overline{\theta}))$ can fully converge to 0. No systematic variance can be generated in the fitting results, $|R(T;\overline{\theta}) - \overline{R}| \lesssim \sigma_{\overline{C}}$, implying a successful restoration of the model-true equilibrium concentrations. However, if nonequilibrium is the proper assumption, then the $f(R(T;\overline{\theta}))$ can converge to a finite value near 0. Under this assumption, measuring the model-true equilibrium requires a limit excess of the experimental configuration, thereby generating an undetectable gap in the fitting results, $|R(T;\overline{\theta}) - \overline{R}| \gg \sigma_{\overline{C}}$. This implies the reconstruction failure of the model-true equilibrium concentration at T, leading to excessive interpretations of the measured protein concentration. Thus, the systematic variance that arises from the double data interpretations cannot be evaluated without computing the dynamical behavior of the equilibrium models.

A computational modeling approach for a whole experimental system is more relevant to extract the impact of various systematic uncertainties [11,12]. In this Rapid Communication, we introduce a comprehensive method to quantitatively evaluate the systematic variance computed not only from a computer simulation of live-cell imaging systems but also image processing and pattern recognition algorithms for biological images. In particular, we construct a bioimage simulation module for an oblique illumination fluorescence microscopy system configured to observe receptor proteins binding to ligands on an apical surface of biological cells. We then show how the nonstatistical variance leads to misidentification of cooperativity in the binding system.

Evaluation method. A key insight into evaluating systematic variance is to estimate how well the ground-true model properties can be restored through analytical procedures, influencing the interpretation of biological properties reconstructed (or extracted) from actual biological images [6–8]. Such model-driven evaluation allows us to quantify the restoration efficiency and defects (or failure) in the reconstruction processes. We cannot fully know the true model; otherwise, there would not be any uncertainty in the biological measurements. However, we can approximately know what to expect either from earlier experimental results or from the biological models derived from experimental knowledge. Such approximations can function as a guide to compute systematic variance in an organized manner from a specific experimental configuration of interest.

Systematic variance generally causes the reconstructed properties to be shifted in one direction from the ground-true model properties [6–8]. Of particular importance is the quantifying of systematic variance that arises from undetectable sources in the measurement processes. If the ground-true property is well restored through the reconstruction process, then it is unchanged and has a weak influence on the biological interpretation. However, if the reconstruction process poorly restores the true property, it may change significantly, affecting the biological interpretation. For example, geometric uncertainties imposed by the unobservable sources such as complex and irregular shapes of membrane-enclosed cellular compartments (e.g., endoplasmic reticulum) in fluorescence recovery after photobleaching (FRAP) experiments lead to invalid measurements of molecular mobility and compartmental connectivity [13,14].

A realistic ground-true model simulation that approximately represents a whole experimental system can be constructed for the model-driven evaluation. Biological measurements using live-cell imaging techniques are generally governed by various natural laws and principles of biochemistry and physics. Models of each imaging process can be simulated within the limited range and dimensions of model-parameter space. Various model-simulation studies exist in physics simulations for molecular fluorescence and optical

apparatus [15–18] and systems biology simulations aimed at explaining and predicting biological phenomenon [19–21]. We integrate these model simulations into a unified model corresponding approximately to a whole experimental system, thus helping to explore the extended dimensions of model-parameter space that can affect potential imaging and analytical outcomes [13,22–28]. In particular, we have developed the bioimage simulation platform for handling a large range of biochemical and physical parameters that govern image-based measurement systems, generating computational photomicrographs that arise from the various systematic sources: spatiotemporal models of biological cells, photophysics, and imaging apparatus [25]. Through such simulation platforms, the biological interpretation of measured properties can be more objectively evaluated and understood under a specific experimental configuration of interest.

Results. The computational method presented here enables us to evaluate the systematic variance that arises from undetectable sources in cooperative binding measurements using fluorescence microscopy. There are two major parts in our work.

First, we program a bioimage simulation module for a single-molecule experimental system using an oblique illumination fluorescence microscope configured to observe biochemical reactions and the aggregation of ligand-induced receptors on an apical region of a cell membrane [25,29–32]. Implementation details are described in Sec. A of the Supplemental Material (SM) [33]. Figure S6 represents the optical arrangement and cell-surface geometry of the cell model illuminated with an incident beam angle less than the critical angle. Microscopy specifications and the operating conditions are also shown in Table S3.

We then evaluate our analytical procedure (see SM Sec. B [33]) to identify the cooperativity in the cell models: simple binding of ligands to single receptors and dimer formations of ligand-enhanced receptors [e.g., epidermal growth factor (EGF) receptors [30,34,35], ErbB receptors [31,32], and membrane-anchored receptors [36]]. There exist a large number of systematic sources in the cooperative binding measurements: for example, the local precision of single molecule images, normalization procedure, and initial concentrations of ligands and receptors. In particular, we focus on computing the systematic uncertainties associated with the image acquisition period and spot-detection efficiency in the measurement process. The evaluation results are summarized in Fig. 1 (see SM Sec. C for more details [33]).

Cooperative characteristics in the receptor aggregation systems can be generally seen in the concavity of the Scatchard plot [37–40]. In simple ligand-receptor binding, the ground-true and the reconstructed Scatchard plots exhibit a straight line that represents no cooperativity, implying successful restoration of the cooperative characteristics by the analytical procedure. A concave downward curve that represents positive cooperativity in dimer formation I is also well conserved by the analysis. However, the concavity of the Scatchard plot for dimer formation II is violated by the reconstruction process. While the ground-true plot is well characterized as a concave upward curve that represents negative cooperativity, the reconstructed plot exhibits positive cooperativity. Qualitative interpretation of the Scatchard

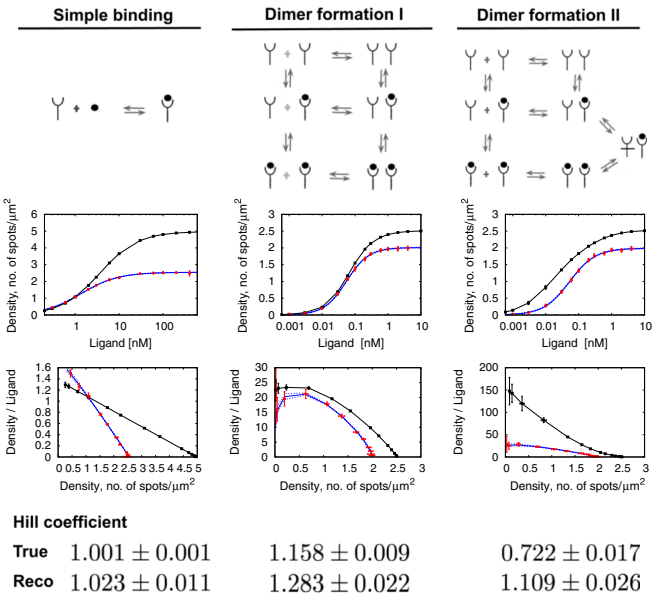

FIG. 1. Summary of the evaluation results. The reconstructed Hill coefficients are compared with the ground-true Hill coefficients. The top row shows the molecular networks: the simple ligand-receptor binding and the dimer formations of the ligand-induced receptors. The Y-shaped object and black solid circle represent the receptor and the ligand, respectively. Y-bar objects represent an intermediate state of the receptor. The equilibrium binding curves and the Scatchard plots are shown in the middle rows. Red and black lines represent the reconstructed and the ground-true data points. Blue solid lines indicate the best-fit curves. The best-fit values and statistical uncertainties (1σ) of the Hill coefficients are shown in the bottom row. If the Hill coefficient is less than unity ($n < 1$), then the receptor system exhibits negative cooperativity. If $n > 1$, then cooperativity is positive. There is no cooperativity if $n = 1$.

plots thus implies misidentification of cooperativity in dimer formation II.

Cooperative characteristics are also found in the shape of the equilibrium binding curve [37–40]. In standard approaches to biological sciences, the Hill function can be fitted to the binding curves to quantify cooperative characteristics in binding systems. The Hill function can be generally written in the form of

$$B(L) = \frac{B_0 L^n}{K_A^n + L^n}, \tag{4}$$

where L, B_0, K_A, and n represent the ligand concentration, maximum area density of ligand binding, ligands occupying half of the binding sites, and the Hill coefficient. The observed area density binned in each ligand concentration input is compared to the expected area density for the Hill function. The best-fit parameters are these which minimize $\chi^2 = -2 \ln \mathcal{L}$ where $\mathcal{L}$ is the likelihood function,

$$\chi^2 = \sum_{i=0}^{N\text{bins}} \frac{(O_i - E_i)^2}{\sigma_i^2}, \tag{5}$$

where O_i and E_i are the observed and expected area densities in the ith input, and σ_i is the statistical error in O_i. In addition,

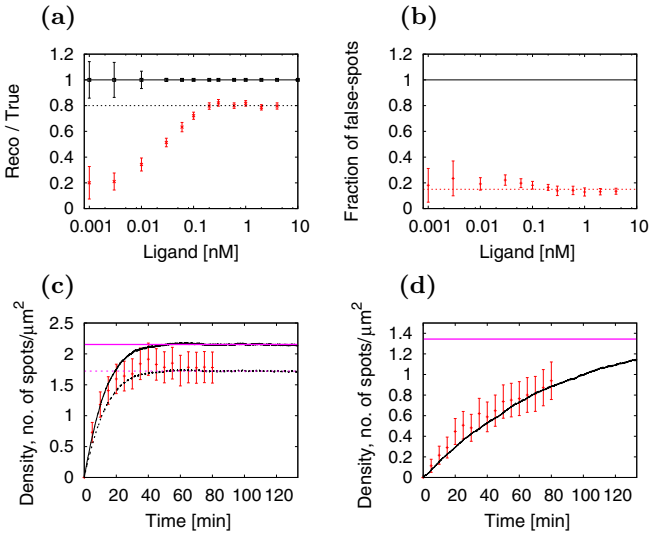

FIG. 2. More properties of dimer formation II. (a) The restoration efficiency of the area density with respect to the concentration range of 1.0 pM to 4.0 nM. The black dashed line represents 80% efficiency. (b) Fractional occupancy of false spots (or defects) with respect to the concentration range. The red dashed line represents 15% occupancy. (c) Time-course data for 0.300 nM ligand input. The reconstructed data are shown by red crosses. Solid and dashed pink lines represent the ground-true equilibrium state and 80% of the true equilibrium state. The ground-true response of the binding state is shown with black solid lines. The 80% restoration of the true response is shown by the dashed black line. (d) Time-course data for 0.030 nM ligand input.

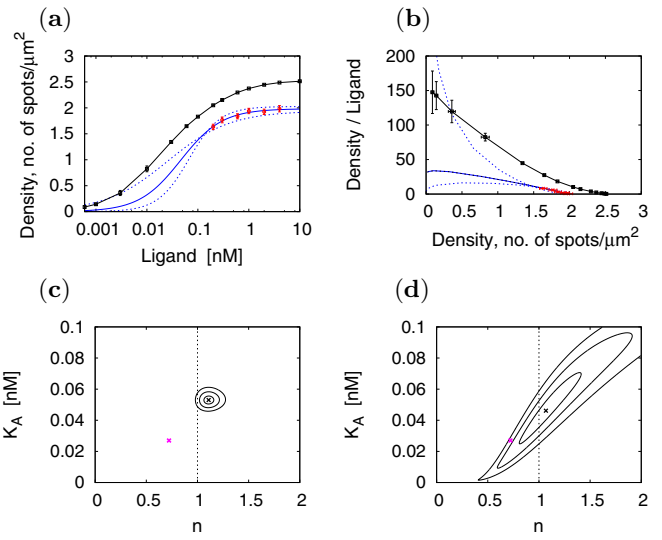

FIG. 3. The fitting results of dimer formation II. (a) The equilibrium binding curve. (b) Scatchard plot. Red and black lines represent the reconstructed and the ground-true data points. Blue solid and dashed lines indicate the best-fit curves and the curves shifted $\pm 1\sigma$ from the best fits, respectively. (c) Confidence levels of data fitting in the full concentration range. (d) Confidence levels of data fitting in the range of high concentration. Pink and black stars represent the ground truth and the best fit, respectively. Black contours around the best fit are allowed at 68%, 95%, and 99% confidence levels.

no penalty terms for nuisance parameters are introduced in this minimization function.

In dimer formation I, the ground-true and the reconstructed binding curves exhibit concave downward curves that represent positive cooperativity ($n > 1$), implying successful restoration of the cooperative characteristics. The unity value of the ground-true Hill coefficient ($n = 1$) in the simple binding is also well conserved by the analysis. However, in the dimer formation II, positive cooperativity appears in the reconstructed curves while the ground-true curve displays that the Hill coefficient is less than unity ($n < 1$), representing negative cooperativity. Hence, the cooperative characteristics are violated by the analytical procedure.

To clearly understand what causes such a violation in dimer formation II, we estimated the restoration efficiency and defects of the analytical procedure. Figure 2(a) shows the ratio of the reconstructed binding curve to the ground-true curve: The shape of the true binding curve is partially restored in the reconstructed curve. While the restoration efficiency of the spot area density is about 80% and steady at relatively higher ligand concentration inputs ($\gtrsim$0.2 nM), the efficiency significantly decreases in the lower ligand concentration region (<0.2 nM). Approximately 13% of detected spots are false and quite steady with respect to the concentration range [see Fig. 2(b)].

In the higher concentration range, the shape of the reconstructed binding curves are unchanged from the ground-true curves. Figure 2(c) shows that the reconstructed responses (red crossed lines) successfully converge to 80% of the true-equilibrium state (pink dashed lines), reaching 80% restoration of the true-equilibrium state. Therefore, imperfect performance of the spot-detection algorithm can shift the entire reconstructed binding curves up and down, implying a weak influence on the identification of cooperativity.

However, in the lower concentration range, the reconstructed responses still remain in a nonequilibrium state within the image acquisition period, 0–5000 s [see Fig. 2(d)]. The responses are so slow that the binding system cannot completely converge to an equilibrium state within the acquisition period. Such a slow transition thus leads to the misidentification of the system's equilibration. Although the true-nonequilibrium binding state (black line) is well restored by the reconstruction procedure, the reconstructed binding state (red crossed lines) fails to converge to the true-equilibrium state (pink line), generating a gap between the reconstructed binding state and the true-equilibrium state. Such gaps cannot be detected even during the acquisition period, thereby leading to a violation of the cooperative characteristics.

Finally, we estimated statistical uncertainties in the fitting parameters to numerically indicate the confidence of our fitting results of dimer formation II [7,8]. Figure 3(c) shows the confidence levels of the fitting result in the full concentration range: The ground truth (pink star) is located outside of the 99% confidence level, implying a failure to restore the true parameter values. In this analysis, the slow transition in the lower concentration range is the major systematic source generating gaps between the reconstructed binding state and the true-equilibrium state. This can cause the restoration failure of the ground-true Hill coefficient. Such systematic gaps cannot be eliminated by even increasing the number of cell samples.

Cooperativity has been generally evaluated under the assumption that the binding systems completely converge to the equilibrium state during the image acquisition period [31,32]. Our results, however, imply the violation of this assumption in dimer formation II. For a proper analysis and interpretation, we performed a parameter fitting in a limited range of ligand concentration, 0.2–4.0 nM (see Fig. 3). The best fit of the Hill coefficient is 1.068 ± 0.36(stat.) while the ground truth is 0.722. Figure 3(d) shows the confidence levels for the fitting result: The ground truth (pink star) is located within the 99% confidence level. While the ground truth of the dimer formation exhibits negative cooperativity, the reconstructed Hill coefficients largely fluctuate around unity. The cooperative characteristics are thus less determinable in this analysis, but the contour line successfully encloses the ground truth, displaying a better result.

Conclusion. Major scientific activities in biological sciences are dedicated not only to extracting laws and patterns from experimental data but also experimentally validating the biological models derived from experimental knowledge [41,42]. Various model candidates can be either confirmed or refuted by repeating these activities. The key to the successful reporting of experimental results is to provide an objective evaluation and representation of the uncertainties that arise from imprecision and inaccuracies in the experimental processes. The study and estimation of the experimental uncertainties have been generally known as an error analysis, its main function being to allow biophysicists to numerically indicate the validity and confidence of their experimental results [6–8].

In the error analysis, a statistical analysis of the experimental data is only half the story. The other half is the computation of the systematic uncertainties that affect the sensitivity and limitation of a given experimental configuration to the model parameters and, even more significantly, to new advancements in biophysics and biology. An identification of the new findings in the experimental approaches must always contend with those error estimations. For this reason, we proposed the computational method to evaluate the impact of various systematic uncertainties in the biological measurements using live-cell imaging techniques. We then presented examples of not only estimating the systematic uncertainties in model assumptions and parameters (e.g., image acquisition periods and spot-detection efficiency) that can affect the cooperative binding measurements but also reducing them to levels allowing for proper conclusions. In the near future, we believe our computational scheme can help bridge the gap between theory and experiment in biological sciences.

Acknowledgments. We would like to thank Yasushi Okada, Tomonobu M. Watanabe, Jun Kozuka, Michio Hiroshima, Kozo Nishida, Kazunari Iwamoto, Yuki Shindo, Hanae Shimo, Yin Fai Chin, Suguru Kato, Toru Niina, Shin Moriga, Taku Tsuzuki, Koji Ochiai, Keiko Itano, Sibel Ozer, Kotone Itaya, and Kaoru Ikegami for their guidance and support throughout this research work. We would also like to thank Yasushi Sako and Kylius Wilkins for their critical reading of the manuscript. This research work is supported by JSPS (Japanese Society for the Promotion of Science) KAKENHI Grant No. 15K12146.

[1] R. D. King, J. Rowland, S. G. Oliver, M. Young, W. Aubrey, E. Byrne, M. Liakata, M. Markham, P. Pir, L. N. Soldatova, A. Sparkes, K. E. Whelan, and A. Clare, The automation of science, Science **324**, 85 (2009).

[2] V. Marx, The big challenges of big data, Nature (London) **498**, 255 (2013).

[3] M. I. Jordan and T. M. Mitchell, Machine learning: Trends, perspectives, and prospects, Science **349**, 255 (2015).

[4] N. Yachie, Robotic Biology Consortium, and T. Natsume, Robotic crowd biology with Maholo LabDroids, Nat. Biotechnol. **35**, 310 (2017).

[5] V. Amrhein and B. Mcshane, Retire statistical significance, Nature (London) **567**, 305 (2019).

[6] L. Geris and D. Gemez-Cabrero, *Uncertainty in Biology* (Springer, Berlin, 2016).

[7] J. R. Taylor, *An Introduction to Error Analysis*, 2nd ed. (University Science Books, Sausalito, CA, 1997).

[8] P. R. Bevington and D. K. Robinson, *Data Reduction and Error Analysis for the Physical Sciences*, 3rd ed. (McGraw-Hill, New York, 2003).

[9] A. C. Babtie, P. Kirk, and M. P. H. Stumpf, Topological sensitivity analysis for systems biology, Proc. Natl. Acad. Sci. USA **111**, 18507 (2014).

[10] P. D. W. Kirk, A. C. Babtie, and M. P. H. Stumpf, Systems biology (un)certainties, Science **350**, 386 (2015).

[11] S. Incerti, G. Baldacchino, M. Bernal, R. Capra, C. Champion, Z. Francis, S. Guatelli, P. Guèye, and A. Mantero, The Geant4-DNA project, Int. J. Model. Simul. Sci. Comput. **1**, 157 (2010); S. Incerti *et al.*, Geant4-DNA example applications for track structure simulations in liquid water: A report from the Geant4-DNA Project, Med. Phys. **45**, e722 (2018).

[12] S. Agostinelli, J. Allison, and K. Amako, GEANT4—a simulation toolkit, Nucl. Instrum. Methods Phys. Res. A **506**, 250 (2003); J. Allison *et al.*, GEANT4 developments and applications, IEEE Trans. Nucl. Sci. **53**, 270 (2006); Recent developments in GEANT4, Nucl. Instrum. Methods Phys. Res. A **835**, 186 (2016).

[13] I. F. Sbalzarini, Modeling and simulation of biological systems from image data, BioEssays **35**, 482 (2013).

[14] J. Mai, S. Trump, I. Lehmann, and S. Attinger, Parameter importance in FRAP acquisition and analysis: A simulation approach, Biophys. J. **104**, 2089 (2013).

[15] J. Lakowicz, *Principles of Fluorescence Spectroscopy* (Springer, Berlin, 2006), p. 954.

[16] J. Pawley, *Handbook of Biological Confocal Microscopy* (Springer, Berlin, 2008), p. 988.

[17] M. Mansuripur, *Classical Optics and its Application* (Cambridge University Press, Cambridge, UK, 2009), p. 714.

[18] B. Valeur and M. Berberan-Santos, *Molecular Fluorescence* (Wiley, Hoboken, NJ, 2012), p. 592.

[19] K. Kaneko, *Life: An Introduction to Complex Systems Biology* (Springer, Berlin, 2006).

[20] U. Alon, *An Introduction to Systems Biology—Design Principles of Biological Circuits* (Chapman & Hall/CRC, Boca Raton, FL, 2007).

[21] M. Tomita, K. Hashimoto, K. Takahashi, T. Shimizu, Y. Matsuzaki, F. Miyoshi, K. Saito, S. Tanida, K. Yugi, and J. Venter, E-CELL: Software environment for whole-cell simulation, Bioinformatics **15**, 72 (1999).

[22] J. Boulanger, C. Kervrann, and P. Bouthemy, A simulation and estimation framework for intracellular dynamics and trafficking in video-microscopy and fluorescence imagery, Med. Image Anal. **13**, 132 (2009).

[23] S. H. Rezatofighi, W. T. E. Pitkeathly, S. Gould, R. Hartley, K. Mele, W. E. Hughes, and J. G. Burchfield, A framework for generating realistic synthetic sequences of total internal reflection fluorescence microscopy images, in *Proceedings of the 2013 IEEE International Symposium on Biomedical Imaging* (IEEE, New York, 2013), pp. 157–160.

[24] J. Angiolini, N. Plachta, E. Mocskos, and V. Levi, Exploring the dynamics of cell processes through simulations of fluorescence microscopy experiments, Biophys. J. **108**, 2613 (2015).

[25] M. Watabe, S. N. V. Arjunan, S. Fukushima, K. Iwamoto, J. Kozuka, S. Matsuoka, Y. Shindo, M. Ueda, and K. Takahashi, A computational framework for bioimaging simulation, PLoS One **10**, e0130089 (2015).

[26] V. Venkataramani, F. Herrmannsdörfer, M. Heilemann, and T. Kuner, SuReSim: Simulating localization microscopy experiments from ground truth models, Nat. Methods **13**, (2016).

[27] M. Lindén, V. Ćurić, A. Boucharin, D. Fange, and J. Elf, Simulated single molecule microscopy with SMeagol, Bioinformatics **32**, 2394 (2016).

[28] M. Weigert, K. Subramanian, S. T. Bundschuh, W. Myers, and M. Kreysing, Biobeam—Multiplexed wave-optical simulations of light-sheet microscopy, PLoS Comput. Biol. **14**, e1006079 (2018).

[29] S. N. V. Arjunan and M. Tomita, A new multicompartmental reaction-diffusion modeling method links transient membrane attachment of E. coli MinE to E-ring formation, Syst. Synth. Biol. **4**, 35 (2010).

[30] Y. Teramura, J. Ichinose, H. Takagi, K. Nishida, T. Yanagida, and Y. Sako, Single-molecule analysis of epidermal growth factor binding on the surface of living cells, EMBO J. **25**, 4215 (2006).

[31] M. Hiroshima, Y. Saeki, M. Okada-Hatakeyama, and Y. Sako, Dynamically varying interactions between heregulin and ErbB proteins detected by single-molecule analysis in living cells, Proc. Natl. Acad. Sci. USA **109**, 13984 (2012).

[32] M. Hiroshima and Y. Sako, Regulation mechanism of ErbB-heregulin interaction shown by single-molecule kinetic analysis in living cells, Biophys. Physicobiol. **53**, 317 (2013).

[33] See Supplemental Material at http://link.aps.org/supplemental/10.1103/PhysRevE.100.010402 for not only updates of different implementations for the fluorescence microscopy simulation module but also details for the model construction and the reconstruction of physical and biological properties.

[34] C. Wofsy, B. Goldstein, K. Lund, and H. S. Wiley, Implications of epidermal growth factor (EGF) induced egf receptor aggregation, Biophys. J. **63**, 98 (1992).

[35] C. Wofsy and B. Goldstein, Interpretation of Scatchard plots for aggregating receptor systems, Math. Biosci. **112**, 115 (1992).

[36] L. Li, G. K. Xu, and F. Song, Impact of lipid rafts on the *T*-cell-receptor and peptide-major-histocompatibility-complex interactions under different measurement conditions, Phys. Rev. E **95**, 012403 (2017); G. K. Xu, J. Qian, and J. Hu, The glycocalyx promotes cooperative binding and clustering of adhesion receptors, Soft Matter **12**, 4572 (2016); G. K. Xu, Z. Liu, X. Q. Feng, and H. Gao, Tension-compression asymmetry in the binding affinity of membrane-anchored receptors and ligands, Phys. Rev. E **93**, 032411 (2016); G. K. Xu, J. Hu, R. Lipowsky, and T. R. Weikl, Binding constants of membrane-anchored receptors and ligands: A general theory corroborated by Monte Carlo simulations, J. Chem. Phys. **143**, 243136 (2015).

[37] C. Goodman, J. Kotz, and K. Sercy, Focus on cooperativity, Nat. Chem. Biol. **4**, 433 (2008).

[38] J. E. Ferrell, Q & A: Cooperativity, J. Biol. **8**, 53 (2009).

[39] M. I. Stefan and N. L. Nove, Cooperative binding, PLoS Comput. Biol. **9**, e1003106 (2013).

[40] R. Phillips, J. Kondev, J. Theriot, H. G. Garcia, and Orme, *Physical Biology of the Cell*, 2nd ed. (Garland Science, Oxford, UK, 2013).

[41] H. Kitano, Systems biology: A brief overview, Science **295**, 1662 (2002); Computational systems biology, Nature (London) **420**, 206 (2002).

[42] P. Godfrey-Smith, *Theory and Reality—An Introduction to the Philosophy of Science* (The University of Chicago Press, Chicago, 2003).